Arabian Journal of Chemistry (2020) 13, 4462–4476

King Saud University

Arabian Journal of Chemistry

www.ksu.edu.sa
www.sciencedirect.com

ORIGINAL ARTICLE

Catalytic performance of $NiFe_2O_4$ and $Ni_{0.3}Zn_{0.7}Fe_2O_4$ magnetic nanoparticles during biodiesel production

António B. Mapossa [a,d,*], Joelda Dantas [a], Manoel R. Silva [b], Ruth H.G.A. Kiminami [c], Ana Cristina F.M. Costa [a], Michael O. Daramola [e]

[a] *Federal University of Campina Grande, Synthesis of Ceramic Materials Laboratory – LabSMaC, Science and Engineering of Materials Postgraduate, Aprígio Veloso Avenue – 882, Bodocongó, Zip Code 58109-970 Campina Grande, PB, Brazil*
[b] *Federal University of Itajubá, Department of Physics, Mailbox: 50, Itajubá, MG 37500-903, Brazil*
[c] *Federal University of São Carlos, Department of Materials Engineering, Zip Code 13565905, São Carlos, SP, Brazil*
[d] *Institute of Applied Materials, Department of Chemical Engineering, University of Pretoria, Private Bag X20, Hatfield 0028, Pretoria, South Africa*
[e] *School of Chemical & Metallurgical Engineering, Faculty of Engineering and the Built Environment, University of the Witwatersrand, Wits 2050, Johannesburg, South Africa*

Received 20 July 2019; accepted 17 September 2019
Available online 25 September 2019

KEYWORDS

Nickel–ferrite;
Nickel–zinc ferrite;
Combustion reaction;
Transesterification reaction;
Biodiesel

Abstract In this study, catalytic performance of nanoferrites $NiFe_2O_4$ and $Ni_{0.3}Zn_{0.7}Fe_2O_4$ is reported. Nickel–ferrite and mixed nickel–zinc ferrite were successfully synthesized by combustion reaction using a conical reactor with production of 10 g per batch. Crystallinity and purity or quantitative analysis of the catalyst were checked by using X-ray diffraction and energy dispersive X-ray analysis. Surface chemistry was examined via Fourier transform infrared (FTIR) analysis; N_2 physisorption at 77 K was conducted to obtain textural properties of the catalyst; a thermogravimetric analysis, a scanning electron microscope and a transmission electron microscopy were used to check the thermal stability and morphology of the catalyst, respectively. The catalysts were used to convert soybean oil into biodiesel in a batch mode and the reaction mixture was analyzed using a pre-calibrated gas chromatograph (GC). The presence of a single-phase spinel structure in the synthesized nanoparticles was confirmed by the XRD results. The $Ni_{0.3}Zn_{0.7}Fe_2O_4$ had a lower surface area value of 71.5 m^2g^{-1} and higher saturation magnetization value of 31.50 emu/g than sample $NiFe_2O_4$ which had 87.6 m^2g^{-1} and 17.85 emu/g, respectively. Biodiesel yield of 94% was obtained

* Corresponding author at: Federal University of Campina Grande, Synthesis of Ceramic Materials Laboratory – LabSMaC, Science and Engineering of Materials Postgraduate, Aprígio Veloso Avenue – 882, Bodocongó, Zip Code 58109-970 Campina Grande, PB, Brazil.
E-mail address: mapossabenjox@gmail.com (A.B. Mapossa).
Peer review under responsibility of King Saud University.

Production and hosting by Elsevier

https://doi.org/10.1016/j.arabjc.2019.09.003

with $Ni_{0.3}Zn_{0.7}Fe_2O_4$ and 49% was obtained with $NiFe_2O_4$. Better performance of $Ni_{0.3}Zn_{0.7}Fe_2O_4$ when compared to that of $NiFe_2O_4$ could be attributed to higher acidity of the former. Findings from this study suggest that the development of nickel-zinc ferrite nanoparticles as magnetic heterogeneous catalysts could provide an environmentally friendly platform for biodiesel production.

1. Introduction

Biodiesel is one the potential renewable energy preferred as an alternative source of energy to petrol-derived diesel. It is biodegradable, non-toxic and could be easily produced through esterification or transesterification processes (Zhang et al., 2016). Alcohol, and triglycerides obtained from vegetable oils and animals fats are the raw materials to produce biodiesel (Lopez et al., 2005).

The conventional catalysts applied in the esterification and transesterification processes to produce biodiesel are homogeneous catalysts. Unfortunately, these catalysts are very difficult to separate from the reaction mixture and must be neutralized and washed at the end of reaction, thereby resulting difficulties in separation and recycling of spent catalysts (Lopez et al., 2005). Therefore, further development of homogeneous catalysts is limited (Liu et al., 2016). The enzymatic esterification and transesterification of triglycerides are an option but suffers from high costs and the unstable behaviour of the various enzymes employed in the process (Degirmenbasi et al., 2015). To solve these problems, heterogeneous catalyst is proposed as a potential class of catalyst to alleviate the aforementioned difficulties. More specifically, heterogeneous catalysts obtained via a green process could be instrumental to reducing emissions of environmental pollutants (Liu et al., 2016).

Various solid catalysts such as metal oxides (Zhao et al., 2018; Xie et al., 2018; Yang et al., 2019; Zhang et al., 2019), composite metal oxides, zeolites, hydrotalcites, anion exchange resins and lipase immobilized on various supports have been tested in different areas in particular for biodiesel production. Among the aforementioned catalysts, ferrimagnetic oxides, or ferrites, are very attractive materials due to their outstanding physical properties and high applicability in nanotechnology (Andjelković et al., 2018). These materials are widely used as industrial ceramics where nanomaterials with improved performances are required because of their excellent electrical and magnetic properties (Sundararajan and Srinivasan, 1991; Goldman, 1993) and considerable chemical and thermal stability. Magnetic properties of ferrites are tightly bound to the position of the divalent cations in the crystal structure. Ferrites crystallize in a spinel structure (cubic space group F*m3d*), where divalent and trivalent cations are arranged among tetrahedral and octahedral sites (Deepty et al., 2019). Magnetic divalent cations (Ni^{2+}) have strong preference for the octahedral sites, and thus, $NiFe_2O_4$ is an inverse spinel. In contrast, diamagnetic divalent cations, such as Zn^{2+}, occupy tetrahedral sites. Therefore, the structure of $ZnFe_2O_4$ is a normal spinel. Due to the opposite path of crystallization, the properties of $NiFe_2O_4$ and $ZnFe_2O_4$ are diametrically different, i.e., $NiFe_2O_4$ is ferrimagnetic with a curie temperature $\approx$ 858 K, while $ZnFe_2O_4$ shows antiferromagnetic ordering below 9 K. The composition of a ferrite can be modified without compromising its basic crystalline structure, indicating that properties of the materials can be easily tuned just by varying the ratio of the divalent cations (Andjelković et al., 2018). Mixed nickel–zinc ferrites has the general site occupancy $(Zn_xFe_{1-x})_{tetrahedral}[Ni_{1-x}Fe_{1+x}]_{octahedral}O_4$, where the composition varies from $NiFe_2O_4$ (x = 0) to $ZnFe_2O_4$ (x = 1), resulting in the redistribution of metal ions over the tetrahedral and octahedral sites and modification of the properties (Costa et al., 2002a; Andjelković et al., 2018).

Preparation methodology is essential for controlling the physical properties of the materials, such as magnetic, electrical and optical (Hajalilou and Mazlan, 2016). On other hand, different methods for the synthesis of nanocrystalline ferrites have been developed to optimize low-cost synthesis material with the desired characteristic ratio (Hajalilou and Mazlan, 2016; Hazra and Ghosh, 2014). A variety of methodologies such as solid-state reaction by microwave (Amiri et al., 2011; Gupta et al., 2007; Liu et al., 2014), sonochemical synthesis (Shafi et al., 1997), citrate precursor (Prasad and Gajbhiye, 1998), sol-gel (Chen and He, 2001), co-precipitation (Shi et al., 1999; Yang et al., 1999), combustion reaction (Dantas et al., 2017), micro-emulsion (Abbas et al., 2017), hydrothermal (Chen et al., 2016), are available in the literature for the synthesis of these spinel nanoferrites with different modifications.

Among the above-mentioned methods, combustion reaction synthesis method has received attention from researchers over recent years to develop nanomaterials (Diniz et al., 2004; Andrade et al., 2005; Syue et al., 2011; Santos et al., 2012; Rezlescu et al., 2013; Gabal et al., 2014; Shanmugavel et al., 2014; Tholkappiyan and Vishista, 2014; Murugesan et al., 2014). This method is suitable for the synthesis and processing of ceramic materials, mainly due to the high purity, short reaction time, rapid and uniform heating, energy saving, high chemical yield and homogeneity of the final products (Cai et al., 2013). The high purity of the material synthesized by this method is attributed to the removal of impurities such as volatile species at elevated temperatures, typically obtained during the reaction (Ping et al., 2009). Moreover, the nanomaterials can be produced in pilot scale of 10, 30, 100, 200 g/batch or more via combustion reaction method (Costa et al., 2009; Costa and Kiminami, 2012).

In catalysis, the magnetic nanoparticles have emerged as valuable alternatives to conventional heterogeneous supports (Abu-Reziq et al., 2006; Shylesh et al., 2009). These materials can act as promising heterogeneous catalysts because the manipulation of the nanoscale structures provides nanocatalysts with a large number of active sites, thereby enhancing their surface area. The advantage to work with this material is that the ferrite, as nanomagnetic solid catalyst, can be easily separated from the reactants by an external magnetic field (magnet). This can effectively prevent loss of the catalyst and increase its recovery rate

during the separation process (Dantas et al., 2017). Thereby reducing the generation of waste and simplifying the processes involved in the chemical reactions. Besides enhanced catalyst separation from the reaction mixture, nanoferrites have high contact area, high thermal stability and good chemical properties. These characteristics have made magnetic nanoparticles promising catalysts for biofuels production.

For biodiesel production, the pioneering research in this field using magnetic nanoparticles was reported by Dantas et al. (2012) and Dantas et al. (2013).

Having reported promising results by Dantas et al. (2012) and Dantas et al. (2013), other researchers have been exploring the use of magnetic nanoparticles for biodiesel production. For instance, Zhang et al. (2014) synthesized $CaO/CoFe_2O_4$ and tested it for soybean oil transesterification into biodiesel. The authors reported enhanced catalytic performance for the catalyst when compared to $CaO/ZnFe_2O_4$ and $CaO/MnFe_2O_4$, with a yield of 87.4% from $CaO/CoFe_2O_4$. In the same vein, Seo et al. (2014) studied effect of different sizes of functionalized particles of barium ferrite ($BaFe_{12}O_{19}$) in microalgae biofuel production with promising results reported by the authors.

Gurunathan and Ravi (2015), also studied the doped copper with zinc oxide as heterogeneous catalyst for methanolic transesterification of frying oil. The obtained results by the authors showed a maximum yield of biodiesel of 97.71% (w/w). Furthermore, (Liu et al., 2016) used $MgFe_2O_4$@CaO as a heterogeneous catalyst for soybean oil biodiesel production, and the authors reported good recovery potential simply by a conventional external magnet without significant decrease in the catalytic activity. In addition, the authors reported that the catalyst displayed good stability and recyclability potential, indicating that development of these catalysts as new heterogeneous catalysts could provide an environmentally friendly way to produce biodiesel.

Against this background, the present study investigated the catalytic performance of $NiFe_2O_4$ and $Ni_{0.3}Zn_{0.7}Fe_2O_4$ nanoparticles in the transesterification of soybean oil into biodiesel. In addition, catalytic properties such as morphology, magnetic, acidity, zeta potential of the nanoferrites were checked and discussed.

2. Experimental

2.1. Materials and methods

The chemicals used for the synthesis of the $Ni_{1-x}Zn_xFe_2O_4$ (x = 0.0 and 0.7 mol of Zn^{2+}) nanoparticles and for the biodiesel production were: nickel nitrate hexahydrate - $Ni(NO_3)_2{\cdot}6H_2O$ (Vetec, 98%), zinc nitrate hexahydrate - $Zn(NO_3)_2{\cdot}6H_2O$ (Vetec, 97%), iron(III) nitrate nonahydrate - $Fe(NO_3)_3{\cdot}9H_2O$ (Vetec, 99%), known as oxidizing agents, urea - $[(NH_2)_2CO]$ (Vetec, 97%) as reducing agent, to form a redox solution and the methanol (99%)was purchased from Sigma-Aldrich.

For the transesterification reaction was used refined soybean oil, purchased in local commerce in Campina Grande/Paraiba-Brazil, whose physic-chemical characteristics comparing to the National Agency of Sanitary Surveillance (ANVISA) values are shown in Table 1.

The $Ni_{1-x}Zn_xFe_2O_4$ nanoparticles with x = 0.0 and 0.7 mols of Zn^{2+} were synthesized by the combustion reaction method (Costa et al., 2002b). For the synthesis, the stoichiometric amounts of metal nitrates with urea were initially mixed in a stainless-steel container made for production of 10 g/batch of the final product and heated in a conical reactor (maximum temperature of around 600 °C) up until self-ignition occurs (combustion) (Costa and Kiminami, 2012; Vieira et al., 2014).

Table 1 Results of the characterization of the refined soybean oil, compared to the expected values taken as reference.

Oil characterization	Calculated value	Established value (ANVISA)
Iodine level (g I_2/100 g)	138.6	120.0–140.0
Acidity level (% oleic acid)	0.06	< 0.3
Specific mass 20 °C (kg/m^3)	921	919–925

The combustion synthesis technique was based on the thermodynamic concepts of the chemistry of propellants and explosives, involving redox reaction mixtures that contain the metal ions of interest, such as oxidizing reagents, and a fuel, usually urea ($CO(NH_2)_2$) or glycine ($C_2H_5NO_2$) as a reducing agent (Vieira et al., 2014). The reducing agent (urea), has proven to be the most convenient fuel to use because it is readily available commercially, is cheap and generates the highest temperature, although fuel-rich mixtures might produce prematurely sintered particle agglomerates (Segadães et al., 1998). According to propellant chemistry, the oxidizing and reducing valences of different elements are as follows: Ni = +2; Zn = +2; Fe = +3; C = +4; H = +1; O = −2. In a urea to nitrate reaction, total reducing valences of urea is +6 and total oxidizing valences of nitrates (Ni$(NO_3)_2$: Fe$(NO_3)_3$; 1:2) or (Ni$(NO_3)_2$: Zn$(NO_3)_2$: Fe$(NO_3)_3$; 0.3:0.7:2) for $NiFe_2O_4$ and $Ni_{0.3}Zn_{0.7}Fe_2O_4$ ferrite, is −40. Therefore, fuel ($CO(NH_2)_2$) – nitrate composition become −40 + 6n = 0; n = 6.67 mol in the reaction. Because it is a complete combustion, the stoichiometric reaction (Φe = 1) follows the definition described for the oxygen balance equals zero. To achieve this, all the oxygen content from the metal nitrates must be completely oxidized by fuel present in the mixture (Hwang et al, 2005). Based on this, chemical reactions for combustion method can be expressed as follows:

(a) $Ni(NO_3)_2{\cdot}6H_2O_{(s)} + 2Fe(NO_3)_3{\cdot}9H_2O_{(s)} + 6.67(NH_2)_2CO_{(s)} \rightarrow NiFe_2O_{4(s)} + 6.67CO_{2(g} + 37.33H_2O_{(g)} + 10.67\ N_{2(g)}$

(b) $0.3Ni(NO_3)_2{\cdot}6H_2O_{(s)} + 0.7Zn(NO_3)_2{\cdot}6H_2O_{(s)} + 2Fe(NO_3)_3{\cdot}9H_2O_{(s)} + 6.67(NH_2)_2CO_{(s)} \rightarrow Ni_{0.3}Zn_{0.7}Fe_2O_{4(s)} + 6.67CO_{2(g)} + 37.33H_2O_{(g)} + 10.67\ N_{2(g)}$

During synthesis, the reaction parameters such as the maximum temperature of the combustion flame (T_{max}) and initial reaction temperature (T_i) were measured using an infrared pyrometer (Raytek, RAYR3I model ± 2 °C). The reaction time (t_r) and the flame time (t_f) were measured using a digital timer (Technos®). The synthesized products were sieved using a mesh #325 ABNT (45 μm).

2.2. Catalyst characterization

The synthesized $NiFe_2O_4$ and $Ni_{0.3}Zn_{0.7}Fe_2O_4$ were characterized using a X-ray diffractometer (model XRD 6000 equipped

with CuKα radiation source, λ = 1.542 Å, a voltage of 40 kV, current of 30 Ma). The crystallite size was calculated from the extension X-ray line (d_{311}) by the secondary diffraction line deconvolution of the polycrystalline cerium (standard), using the Debye- Scherrer Eq. (1) (Klung and Alexander, 1962):

$$D = \frac{K\lambda}{\beta cos\theta} \quad (1)$$

where λ is the wavelength of X-ray beam, β is full width at half maximum (FWHM) and θ is Bragg scattering angle and K (=0.89) is shape factor.

The theoretical lattice parameter (α_{th}) was calculated using the following relation, represented by Eq. (2) (Satheeshkumar et al., 2019; Bajorek et al., 2019):

$$\alpha_{th} = \frac{8}{3\sqrt{3}}\left[R_A + \sqrt{3}R_B\right] \quad (2)$$

where R_A and R_B are tetrahedral and octahedral bond lengths. But $R_A = r_A + r\,(O)$ and $R_B = r_B + r\,(O)$, here r_A and r_B are the ionic radii of tetrahedral and octahedral sites and r (O) is the radius of oxygen ion (1.32 Å).

Furthermore, the estimation of X-ray density of the ferrite samples was done using Eq. (3) (Deepty et al., 2019):

$$\rho_x = \frac{8M}{N_A\alpha^3} \quad (3)$$

where M, N_A and a are sample's molecular weight, Avogadro's number and experimental lattice constant, respectively.

The quantitative analysis of the elements (Ni, Zn, Fe and O) in $NiFe_2O_4$ and $Ni_{0.3}Zn_{0.7}Fe_2O_4$ samples was carried out with an energy dispersive X-ray analysis (EDX), model EDX-720, Shimadzu®.

Fourier transform infrared (FTIR) spectra of $NiFe_2O_4$ and $Ni_{0.3}Zn_{0.7}Fe_2O_4$ samples were recorded on a Perkin-Elmer Spectrum 100 fitted with the universal attenuated total reflection (ATR) sampling accessory. The FTIR spectra were recorded in absorbance units in the wavenumber range from 4000 to 400 cm^{-1} at a resolution of 4 cm^{-1}. The reported spectra represent averages of 16 scans.

The thermal stability of the synthesized catalysts was determined using thermogravimetric analysis (TGA) on a TA Instruments SDT-Q600 Simultaneous TGA/DSC. Samples weighing approximately 40 mg were heated from ambient temperature up to 800 °C at a rate of 10 °C.min^{-1}. The purge gas was nitrogen flowing at 50 mL min^{-1}. The weight loss was recorded as a function of temperature.

The specific surface area of $NiFe_2O_4$ and $Ni_{0.3}Zn_{0.7}Fe_2O_4$ samples was determined using the method developed by Brunauer, Emmett and Teller (BET) by gas adsorption using a porosimeter, model 3200E YOUNG, Quantachrome®. The particle sizes (equivalent spherical diameters) were calculated using the Reed Eq. (4) (Reed, 1995). The pore volumes and pore diameters were determined by the theory developed by Brunauer, Joyner and Halenda (BJH).

$$D_{BET} = \frac{6}{DS_{BET}} \quad (4)$$

where D_{BET} is the diameter (nm), S_{BET} is the surface area determined by the BET method (m^2/g), ρ is the theoretical density (g/cm^3) and 6 is an experimentally calculated factor implemented for spherical particles with no roughness.

The zeta potential, acidity characterization by TPD of NH_3 were also determined, and the pH was measured using a portable pH meter HOMIS® H004-030, operating in the range from 0 up to14.

The magnetic property of $Ni_{1-x}Zn_xFe_2O_4$ (x = 0.0 and 0.7 mol of Zn^{2+}) was determined from a vibrating sample magnetometer (VSM), model 7404 by Lake Shore, with a maximum magnetic field of 13.700 G at room temperature. With the $M \times H$, it was possible to determine some magnetic parameter such as saturation magnetization (M_s), remanent magnetization (M_r) and coercive field (H_c) of $M \times H$ hysteresis curve. The saturation magnetization was also determined by fitting the field data to the function represented by Eq. (5) as follows:

$$M = M_s\left(1 - \frac{\alpha}{H}\right) \quad (5)$$

where M is the magnetization, Ms is the saturation magnetization, α is the fitting parameter and H is the applied field.

Surface morphology of nickel ferrite and mixed nickel-zinc ferrite samples were evaluated by scanning electron microscopy (Shimadzu Corporation - Superscan SSX-550 SEM-EDX). The small quantity of powders was placed onto carbon tape on an aluminum sample holder. Excess ferrites powders were removed using a single compressor air blast. The samples were coated six times with carbon using an Emitech K950X sputter coater prior to analysis. Furthermore, the morphological aspect of the samples was also evaluated by transmission electron microscope (TEM), HRTEM Model: JEM-3010, JEOL-300 kV.

The active sites analysis was performed via the temperature programmed desorption (TPD) method using NH_3 molecules. In NH_3-TPD studies, the solid, previously equilibrated with a gas under well-defined temperature and partial pressure conditions, is subjected to a heating under temperature and flow schedule of an inert gas, that is, a flow gas that flows out on the sample, by monitoring the continuous gas desorption.

2.3. Catalyst testing in biodiesel production

The catalytic performance of $NiFe_2O_4$ and $Ni_{0.3}Zn_{0.7}Fe_2O_4$ during biodiesel production was evaluated during the transesterification of soybean oil into biodiesel in the presence of methanol (as an alcoholysis agent). This process has been widely used to reduce the high viscosity of triglycerides. As, the transesterification reaction is a reversible reaction of triglycerides with an alcohol (e.g. methanol) to produce methyl-esters and glycerin. The reaction of transesterification includes three steps. First, triglycerides react with methanol (step I) to produce methyl-esters and diglycerides which further react with methanol (step II) (d) to produce methyl-esters and monoglycerides. Finally, the monoglycerides react with methanol to give glycerin and methyl-esters (step II) (Barakos et al., 2008).

$$\text{Triglycerides} + \text{MeOH} \leftrightarrow \text{Diglycerides} + \text{Methyl-esters} \quad (I)$$

$$\text{Diglycerides} + \text{MeOH} \leftrightarrow \text{Monoglycerides} + \text{Methyl-esters} \quad (II)$$

$$\text{Monoglycerides} + \text{MeOH} \leftrightarrow \text{Glycerin} + \text{Methyl-esters} \quad (III)$$

If the oil contains free fatty acids, the esterification reaction of free fatty acids with methanol to produce water and methyl-esters according to equation (IV) below takes place in parallel with transesterification reactions:

$$\text{Free fatty acids} + \text{MeOH} \leftrightarrow \text{H}_2\text{O} + \text{Methyl-esters} \quad \text{(IV)}$$

In this study, for the transesterification reaction, 10 g of soybean oil was used as the feed and the catalyst loading was 2 wt% of the oil. The alcohol to oil ratio, the reaction temperature and reaction time for the reaction were 12:1, 180 °C, and 1 h, respectively.

At the end of each reaction, the catalyst samples were separated by a magnetic field and kept for later use. After the nanocatalysts were separated, the mixture (methyl ester and glycerol) was separated using a separating funnel and washed using a distilled water. In addition, the biodiesel samples were centrifuged for 40 min at 9000 RPM to facilitate complete separation of the components by sedimentation. The biodiesel was analyzed using a pre-calibrated gas chromatography (VARIAN 450c model) equipped with flame ionization detector (FID). The initial temperature for the injection was at 100 °C and the oven was set at 180 °C. The detector operated at a temperature of 380 °C.

The yield was calculated using the amount of biodiesel produced (M_b) divided by the amount of oil (M_o), according to the Eq. (6):

$$R(\%) = \frac{M_b}{M_o} \times 100 \quad (6)$$

3. Results and discussion

3.1. Measurement of reactional parameters

Table 2 lists the combustion synthesis parameters for the $Ni_{1-x}Zn_xFe_2O_4$ (x = 0.0 and 0.7 mol of Zn^{2+}). The system with high concentration of Zn^{2+} (x = 0.7 mol of Zn^{2+}) favored a rise in the maximum temperature by 6% and a reduction of the flame time by 70% compared to values obtained with the x = 0.0 sample. In addition, the Zn^{2+} ions affected in the reduction of the reaction time and flame combustion time. This behavior was attributed to the low heat of formation of zinc nitrate ($\Delta Hf^\circ = -551.30$ kcal/mol) compared to the heat of formation of nickel nitrate ($\Delta Hf^\circ = -528.60$ kcal/mol). Previous study conducted by Zhang and Stangle (1994) reported that the temperature and combustion reaction time are determined primarily by the transition phase, which is an intrinsic characteristic of each system and varies depending on material type.

Additionally, in this study the amount of the reaction products obtained by combustion synthesis was an average of 14 g/reaction. This suggests that there is a good reproducibility of product synthesized by combustion method since the container was designed to produce 10 g/batch of final product (Costa and Kiminami, 2012; Vieira et al., 2014). The nature of reducing agent and quantity of chemicals and type of container used for combustion synthesis also affect the temperature and combustion time. These parameters are most important in the combustion reaction because in most cases they determine the characteristics of the final product (Costa et al., 2003; Segadães et al., 1998).

3.2. X-ray diffraction (XRD) of the catalyst

Fig. 1 shows the X-ray diffraction patterns of the $NiFe_2O_4$ and $Ni_{0.3}Zn_{0.7}Fe_2O_4$. The powder XRD patterns for samples $NiFe_2O_4$ and $Ni_{0.3}Zn_{0.7}Fe_2O_4$ showed the characteristic peaks for the spinel structure. The d-values and intensities of the diffraction agree with literature data of $NiFe_2O_4$ (JCPDF 10-0325) and $Ni_{0.3}Zn_{0.7}Fe_2O_4$ (JCPDF 52-0278). The X-ray diffraction patterns show broad peaks indicating the ultrafine nature and small crystallite size of the particles. It is important to note that no other phases were detected. The most intensive diffraction peaks that correspond to the characteristic crystallographic planes of the spinel structure of ferrites [(2 2 0), (3 1 1), (4 0 0), (5 1 1), (4 4 0)] can be seen in Fig. 1.

The crystallite size and the crystallinity of the samples are shown in Table 3. The crystallite size increased slightly with the addition of Zn^{2+} ions, varying between 13 nm for $NiFe_2O_4$ to 20 nm for $Ni_{0.3}Zn_{0.7}Fe_2O_4$. Thus, the results are proving the efficiency of the combustion reaction process for nanomaterials obtained. The high crystallite size of $Ni_{0.3}Zn_{0.7}Fe_2O_4$ obtained may be attributed to the larger ionic radii of Zn^{2+} compared to the ionic radii of Ni^{2+} ($RZn^{2+} = 0.84$ Å and $RNi^{2+} = 0.74$ Å) (EL-Sayed, 2002). A larger ionic radius makes the particles more strongly bound to each other causing an increase in agglomeration state. Previous study conducted by Zhong et al. (2006) reported that the variation of crystallite

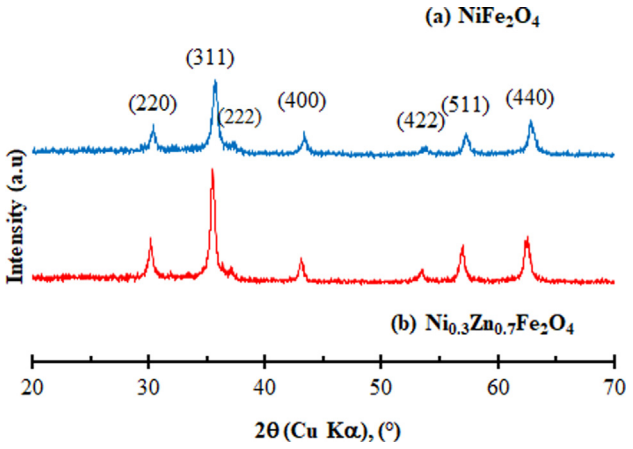

Fig. 1 X-ray diffraction patterns of synthesized (a) $NiFe_2O_4$ and (b) $Ni_{0.3}Zn_{0.7}Fe_2O_4$ ferrites.

Table 2 Parameters evaluated during the combustion reaction of the $NiFe_2O_4$ and $Ni_{0.3}Zn_{0.7}Fe_2O_4$ ferrites.

Sample	T_i (°C)	T_{max} (°C)	$t_{r\ (s)}$	$t_{ch\ (s)}$	$m_{r\ (g)}$
$NiFe_2O_4$	272 ± 8	648 ± 27	658.8 ± 179.4	29 ± 1	15.6 ± 1.2
$Ni_{0.3}Zn_{0.7}Fe_2O_4$	293 ± 3	693 ± 77	538.8 ± 63.0	17 ± 8	12.9 ± 0.8

size for $Zn_{0.32}Mn_{0.60-x}Ni_xFe_{2.08}O_4$ was attributed to the ionic radius of the constituent metals (Zn^{2+}, Mn^{2+} and Ni^{2+}).

Džunuzović et al. (2015) synthesized by combustion method the system $Ni_{1-x}Zn_xFe_2O_4$ system (x = 0.0; 0.3; 0.5; 0.7; 1.0). The results showed the increase of crystallite size from 38 to 45 nm. To achieve this, the authors used the hydrated acetic acid as fuel and 25% of ammonium hydroxide. Sutka et al. (2012) investigated the $Ni_{1-x}Zn_xFe_2O_4$ ferrites (x = 0.0; 0.5 and 1.0) by spray pyrolysis and reported that the crystallite size was around 18.8–22.9 nm. Gao et al. (2013) evaluated the structural and magnetic properties of the $Ni_{1-x}Zn_xFe_2O_4$ system (x = 0.0; 0.5 and 1.0) synthesizing the system by sol-gel method. Their results showed that the crystallite size varied between 24.2 and 65 nm. Furthermore, Azadmanjiri. (2008) synthesized $Ni_{1-x}Zn_xFe_2O_4$ with x = 0.0; 0.1; 0.2; 0.3, 0.4 mol of Zn^{2+} via sol-gel method, the crystallite size of the particles obtained varied between 73 and 80 nm. However, the crystallite sizes reported by these authors were higher compared to the values obtained in this present study which varied between 13 and 20 nm. The results obtained in this current study suggests that the results are better than the results found in the literature once it was possible obtain the synthesized in pilot-scale and nanoparticles via combustion reaction.

The crystallinity of the products varied between 55% for $NiFe_2O_4$ and 72% for $Ni_{0.3}Zn_{0.7}Fe_2O_4$. The addition of x = 0.7 mol of Zn^{2+} in the $Ni_{1-x}Zn_xFe_2O_4$ system indicated that the final products were more crystalline and nanosized. This may also be associated with the increase in the combustion flame temperature.

Furthermore, the experimental and theoretical lattice parameters (α), experimental density obtained by helium pycnometer and estimation X-ray density for $NiFe_2O_4$ and $Ni_{0.3}Zn_{0.7}Fe_2O_4$ are listed in Table 3. It was observed that the value of the theoretical lattice parameter is close to the experimental lattice parameter. Also, the experimental density obtained by helium pycnometer are in reasonable agreement to the estimation X-ray density. The experimental and theoretical density for $NiFe_2O_4$ ferrite were higher than experimental and theoretical density $Ni_{0.3}Zn_{0.7}Fe_2O_4$, this behavior causes an increase in the experimental and theoretical lattice parameters for $Ni_{0.3}Zn_{0.7}Fe_2O_4$. This behavior may be explained to the lattice parameter of these nanoparticles that depends on the radius of Zn^{2+} and Ni^{2+} ions. The radius of Zn^{2+} (0.82 Å) is larger than that of Ni^{2+} (0.78 Å). Therefore, the increase in lattice parameter with decreasing Ni^{2+} content is due to the replacement of the smaller Ni^{2+} cation by the larger Zn^{2+} cation (Ajmal and Maqsood, 2007; Gul et al., 2008; Shahane et al., 2010; Andjelković et al., 2018). Previous studies conducted by Chatterjee et al. (1993) reported that a variation of density for nickel–zinc ferrite also depends on factors such as temperature, synthesis time, processing method, type and quantity of chemicals used for synthesis. On other hand, the synthesis procedure determines the structural and microstructural characteristics of the materials, such as cation distribution, particle size and kinds of defects (De Medeiros et al., 2017; Andjelković et al., 2018).

3.3. Energy dispersive X-ray analysis (EDX)

Table 4 reports values of the elemental analysis obtained from (EDX) and the nominal for $NiFe_2O_4$ and $Ni_{0.3}Zn_{0.7}Fe_2O_4$ ferrites samples. The EDX analysis is indicating the quantitative presence of Ni, Zn, Fe and O in the samples. From the EDX it is clear that no extra impurities are present in $Ni_{0.3}Zn_{0.7}Fe_2O_4$ sample, however small impurities corresponding 0.13% of Si and 0.02% of S are present in $NiFe_2O_4$. The results show that the values of elemental analysis obtained from (EDX) are in close agreement with the nominal for $NiFe_2O_4$ and $Ni_{0.3}Zn_{0.7}Fe_2O_4$.

3.4. Fourier transform infrared (FTIR) spectra

FTIR spectra of the $NiFe_2O_4$ and $Ni_{0.3}Zn_{0.7}Fe_2O_4$ ferrites are shown in Fig. 2. Spinel ferrites are showed with two interstitial sites of tetrahedral (A) and octahedral (B) sites. Waldron. (1955)proposed that the vibrational frequency (υ_1) around 600–500 cm^{-1} is related to the Fe^{3+}–O^{2-} complex at the tetrahedral site (A). The vibrational frequency (υ_2) around 450–350 cm^{-1} is related to the Fe^{3+}–O^{2-} and M^{2+}–O^{2-} complexes (where M^{2+} = Zn^{2+}, Mn^{2+}, Fe^{2+}, etc.) at octahedral

Table 3 Crystallinity and average crystallite size, experimental and theoretical lattice parameters (α), experimental density obtained by helium pycnometer and estimation X-ray density of the $NiFe_2O_4$ and $Ni_{0.3}Zn_{0.7}Fe_2O_4$ ferrites.

Samples	Crystallinity (%)	$D_{(XRD)}$ (nm)	α (Å)	α_{th} (Å)	$\rho_{(Pycnometer)}$ (g/cm^3)	ρ_x (g/cm^3)
$NiFe_2O_4$	55 ± 0.2	13 ± 0.4	8.320	8.337	5.362	5.373
$Ni_{0.3}Zn_{0.7}Fe_2O_4$	72 ± 0.1	20 ± 0.3	8.464	8.413	5.330	5.334

Table 4 Values of the elemental analysis obtained from (EDX) and the nominal for $NiFe_2O_4$ and $Ni_{0.3}Zn_{0.7}Fe_2O_4$ ferrites samples.

Element (%)	$NiFe_2O_4$*		$Ni_{0.3}Zn_{0.7}Fe_2O_4$	
	Nominal	Analysis	Nominal	Analysis
Ni	25.04	25.10	7.37	6.16
Zn	#	#	19.14	17.32
Fe	47.65	47.36	46.72	49.38
O	27.30	27.38	26.77	27.14

The sample $NiFe_2O_4$ does not contain ion Zn^{2+} in its structure.
* 0.02% impurities of S and 0.13% impurities of Si were observed in $NiFe_2O_4$.

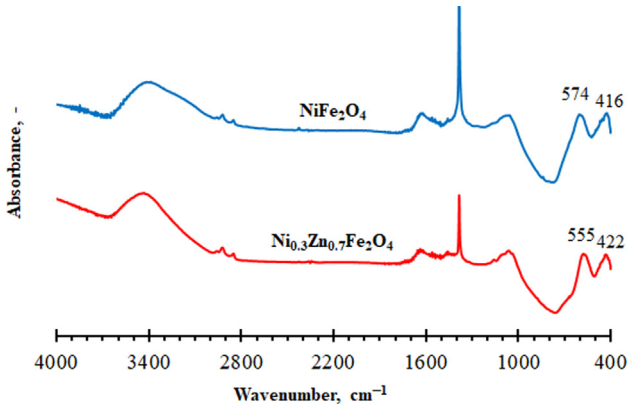

Fig. 2 FTIR spectra of the nickel ferrite and mixed nickel-zinc ferrite samples.

(B) site. In this work, the bands at 574 cm^{-1} and 416 cm^{-1} represents tetrahedral and octahedral modes of $NiFe_2O_4$ while the bands at 555 cm^{-1} and 422 cm^{-1} represented tetrahedral and octahedral modes of $Ni_{0.3}Zn_{0.7}Fe_2O_4$, respectively.

3.5. Thermogravimetric analysis (TGA)

Fig. 3 shows the thermal behaviour of the prepared $NiFe_2O_4$ and $Ni_{0.3}Zn_{0.7}Fe_2O_4$ samples. The combustion reaction method is investigated by thermal analysis (TGA/DTG) of the obtained samples. The TGA/DTG curves thermal decomposition process consist of the following three stages for both samples. The first stage takes place at the temperature range of 31–221 °C and 31–200 °C for $NiFe_2O_4$ and $Ni_{0.3}Zn_{0.7}Fe_2O_4$, respectively. This is explained due to the initial breakdown of the complex and a spontaneous combustion and evaporation of absorbed water (Sivakumar et al., 2011). The spontaneous combustion is caused by interactions of nitrate ions and urea with liberation of H_2O, CO_2 and N_2 as the nitrate ions provided an oxidizing environment for the combustion of the organic components (Sivakumar et al., 2011; Guo et al., 2010). The second weight loss region between 221 and 417 °C and 200–445 °C for $NiFe_2O_4$ and $Ni_{0.3}Zn_{0.7}Fe_2O_4$, respectively are attributed to the continuing oxidation of the organic matters and decomposition of inorganic salts (Nyutu et al., 2008; Zhang et al., 2007). The third stages at the temperature range of 417–530 °C and 445–550 °C for $NiFe_2O_4$ and $Ni_{0.3}Zn_{0.7}Fe_2O_4$, respectively are believed to be due to the formation of corresponding metal oxide (Sivakumar et al., 2011). At a temperature above 550 °C, there is no weight loss, indicating completation of thermal decomposition and formation of spinel nickel ferrite and mixed nickel-zinc ferrite.

3.6. Textural characterization via N_2 adsorption/desorption at 77 K

Fig. 4 shows the adsorption/desorption isotherms of the magnetic nanocatalysts $NiFe_2O_4$ and $Ni_{0.3}Zn_{0.7}Fe_2O_4$. The samples presented the same type of isotherm type V, typical of mesoporous materials, which the main characteristic is a hysteresis loop, and the lack of limitation of nitrogen adsorption at high values of P/P_0 (Sing et al., 1985). Regarding the hysteresis forms, the samples had had a type 3 hysteresis loop (H3), which is characterized by different evaporation and condensation paths between the adsorption and desorption processes sustained by the adsorbent material (Sing et al., 1985; Korichi et al., 2012) and constitute a pore formation with wedge, cone or parallel plate forms. Those characteristics suggest that the samples display the multilayer formation and presence of interparticle mesopores, i.e., pores originated due to the agglomeration of small crystallites (Korichi et al., 2012). Previous studies conducted by Koekkoek et al. (2012) and Rouquerol et al. (1999) reported that the pores are classified according to the following size ranges: micropores when the diameter is less than 2 nm, mesopores when the diameter is ranged between 2 and 50 nm, and macropores when the diameter is larger than 50 nm. Therefore, in this study, the samples investigated are mesoporous materials, i.e., the pores diameters of the samples are in the range 2 to 50 nm.

Table 5 shows the results of the textural parameters calculated from the isothermal adsorption/desorption data. The surface area (BET) of the sample $NiFe_2O_4$ was higher compared

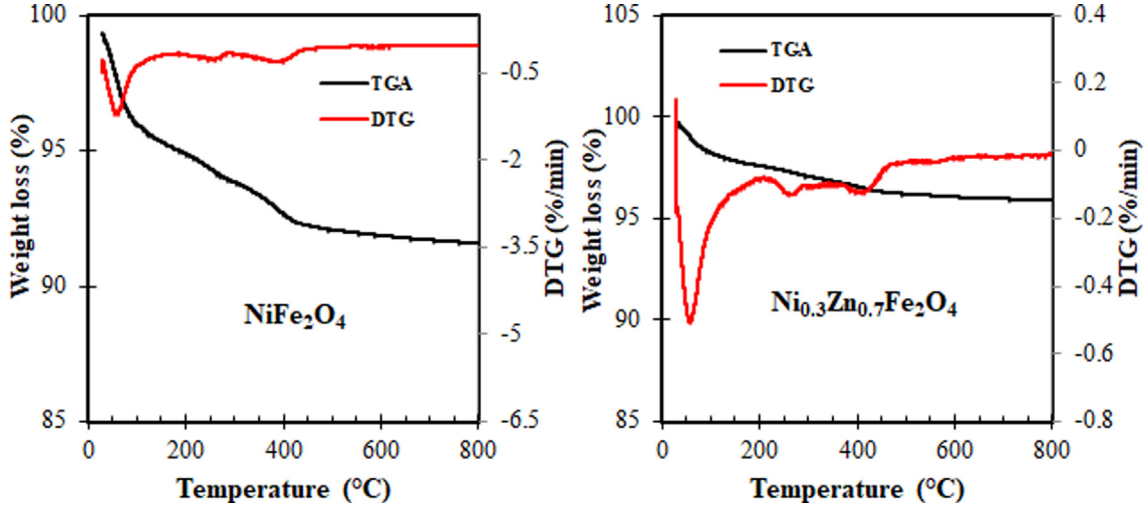

Fig. 3 Thermogravimetric analysis (TGA/DTG) curves of the $NiFe_2O_4$ and $Ni_{0.3}Zn_{0.7}Fe_2O_4$ ferrites.

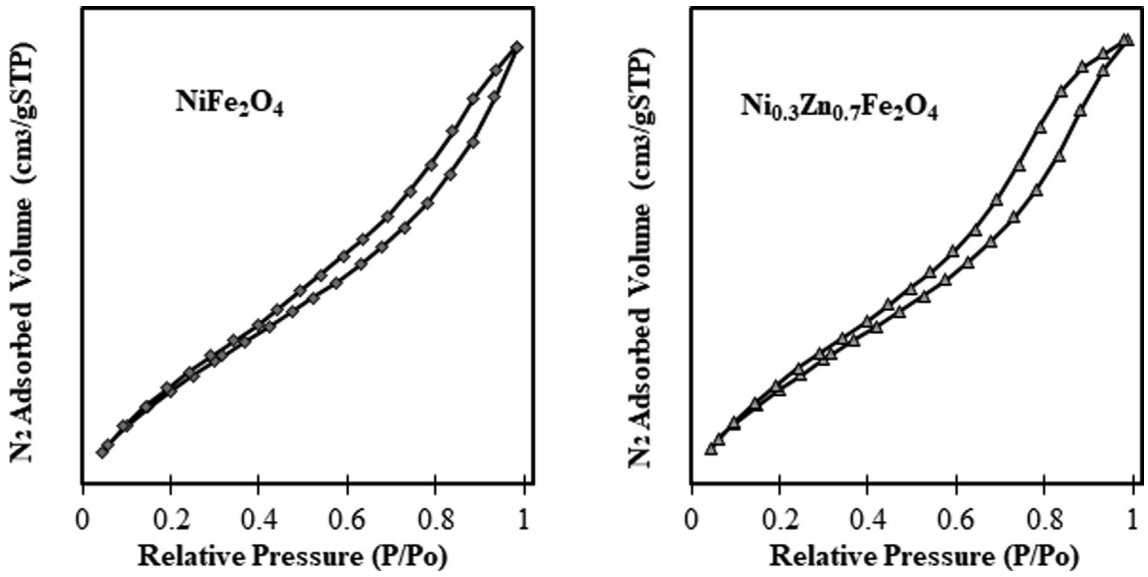

Fig. 4 Adsorption/desorption isotherms of the $NiFe_2O_4$ and $Ni_{0.3}Zn_{0.7}Fe_2O_4$ nanocatalysts.

Table 5 Values of surface area (S_{BET}), particle size (D_{BET}), pore volume (Vp), Pore radius (Dv) and pore diameter (Dp) of the $NiFe_2O_4$ and $Ni_{0.3}Zn_{0.7}Fe_2O_4$ samples.

Samples	S_{BET} (m^2g^{-1})	D_{BET} (nm)	Vp (cm^3/g)	Dv (Å)	Dp (nm)	D_{BET}/Tc[a]
$NiFe_2O_4$	87.6 ± 0.4	12 ± 0.1	0.185 ± 0.04	32.30 ± 0.31	3.397 ± 0.32	0.92
$Ni_{0.3}Zn_{0.7}Fe_2O_4$	71.5 ± 0.2	17 ± 0.3	0.170 ± 0.02	39.4 ± 0.43	3.952 ± 0.34	0.85

[a] Tc = crystallite size.

Table 6 Zeta potential and pH measurements of the $NiFe_2O_4$ and $Ni_{0.3}Zn_{0.7}Fe_2O_4$ ferrites.

Samples	Zeta Potential (mV)	pH
$NiFe_2O_4$	−28.90 ± 0.24	10.0 ± 0.02
$Ni_{0.3}Zn_{0.7}Fe_2O_4$	12.67 ± 0.54	5.80 ± 0.04

to $Ni_{0.3}Zn_{0.7}Fe_2O_4$. This behavior may be explained due to the increasing of maximum combustion temperature as a result of high concentration of Zn^{2+} in the system $Ni_{1-x}Zn_xFe_2O_4$, which this caused the highest crystals growth. On the other hand, the ions of Zn^{2+} have a larger ionic radii compared to those of Ni^{2+} (RZn^{2+} = 0.84 Å and RNi^{2+} = 0.74 Å), thus, this affects the spinel lattice expansion resulting in a smaller grouping of atoms with greater volume, which tends to increase the particle size (Gao et al., 2013; EL-Sayed, 2002). The particle size values size (12 and 17 nm, respectively), are in close agreement with the results obtained for the crystallite since the zinc addition favored its increase, reducing thus the specific surface area as described previously above. In addition, it was calculated the values of ratio particle size/crystallite size (D_{BET}/Tc) for both samples. However, it is known that as closer to 1 (unity) is this ratio, further suggests that the particle size is close to the crystal size, thus indicating that the particle tends to be monocrystalline (Dantas et al., 2017). However, it was observed that the both samples $NiFe_2O_4$ and $Ni_{0.3}Zn_{0.7}Fe_2O_4$ ferrites investigated had lower values than 1 (unity), that is, they are very fine (nanometer), this can be justified based on the analysis of crystallite size, which is determined by the basal width of the diffraction peaks at half height as Debye- Scherrer Eq. (1) (Klung and Alexander, 1962). Because when there are very nanometer samples, the baseline is very broad and peaks are overlapping, introducing a substantial error in the calculation proposed for the crystallite size considering the half height and the width of the peaks (Dantas et al., 2017). Although the surface area of sample $NiFe_2O_4$ was higher than $Ni_{0.3}Zn_{0.7}Fe_2O_4$, in general it could be concluded that both samples possess high surface area.

3.7. Zeta potential and pH

Table 6 presents the zeta potential and pH of the $NiFe_2O_4$ and $Ni_{0.3}Zn_{0.7}Fe_2O_4$. The zeta potential became more positive with an increase in zinc concentration, thereby promoting an increase of the strength of acid sites. It can also be observed that the variation of zeta potential with pH indicates a tendency of negative surface charges in the pH range. On the other hand, the suspension of the sample x = 0.7 showed positive surface charge of the average value of pH = 5.80 in P. Z = 12.67 mV. This indicated that the sample is more acidic while sample x = 0.0 had the highest pH of 10 in P. Z = −28.9 mV, indicating that it is a basic sample. This difference in the pH values can be related to the different capacity of protonation for the different surfaces of nanoparticles in suspension (Feitoza et al., 2014). However, the degree of the zeta

potential provides a suggestion towards the potential stability and effective surface charge of the nanocatalysts. According to the results obtained in this current study, it suggests the excellent stability and positive potential of the nanocatalyst $Ni_{0.3}Zn_{0.7}Fe_2O_4$.

3.8. Magnetic property via VSM

Fig. 5 illustrates the magnetic behavior of the $NiFe_2O_4$ and $Ni_{0.3}Zn_{0.7}Fe_2O_4$ ferrites. It was observed for all samples the ferrimagnetic characteristic behavior of soft magnetic material,

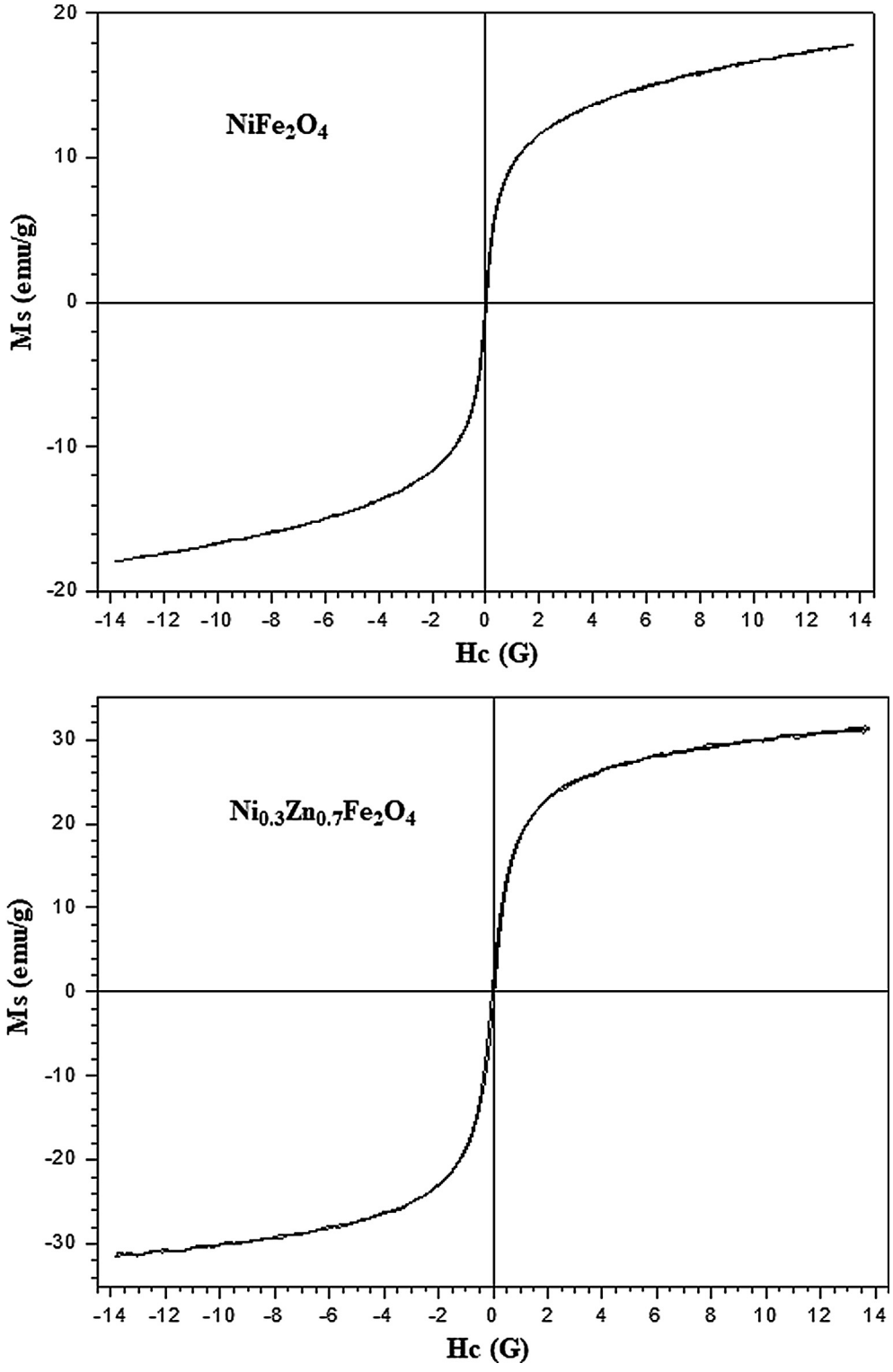

Fig. 5 Hysteresis curves M × H of the $NiFe_2O_4$ and $Ni_{0.3}Zn_{0.7}Fe_2O_4$ ferrites with their respective magnifications to determine the Mr and Hc.

that is, non-permanent magnetic materials which is magnetized and demagnetized very easily with low field values due to their small values of remnant magnetization (M_r) and coercivity (H_c) but different from zero, thus showing complete formation of the narrow magnetic hysteresis loop. It is known that the magnetic ferrites properties are highly dependent of the structure, composition, defects, crystallites size, internal stress and the cations distribution. According to classical literature a demagnetizing field to be considered a soft magnetic material shall be below 10 A/m (Dantas et al., 2017; O'handley, 2000; Morrish, 1995; Derek, 1998; David, 1998; Buschow and De Boer, 2003).

Table 7 reports the results of the magnetic parameters measurement as saturation magnetization (Ms), remnant magnetization (Mr) and coercive field (Hc) of the samples $NiFe_2O_4$ and $Ni_{0.3}Zn_{0.7}Fe_2O_4$ determined from hysteresis curves. Interestingly, the $NiFe_2O_4$ ferrite had lower saturation magnetization (Ms) and remnant magnetization (Mr) than $Ni_{0.3}Zn_{0.7}Fe_2O_4$ ferrite. In addition, the saturation magnetization of the $Ni_{0.3}Zn_{0.7}Fe_2O_4$ ferrite was not much higher, this was approximately 32 emu/g. This behavior may be explained due a high concentration of diamagnetic Zn^{2+} ions in the tetrahedral sites that can cause the weakening of the magnetic moment in the tetrahedral sites promoting spin canting effect, which leads to a drastic reduction in the total magnetization of the spinel lattice (Gorter, 1954; Bercoff and Bertorello, 2000). However, the magnetic properties depend on various factors such as the size, shape and cations distribution (Das et al., 2016). Masrour et al. (2014) they mentioned that the magnetization behavior can be explained based on changes in the exchange interactions between the tetrahedral and octahedral subnets due to crystallinity, particle form and magnetization direction.

As previously reported that the magnetic nature of ferrites is dependent on the method of their synthesis, the distribution of cations between the interstitial tetrahedral and octahedral sites but also on the microstructure and the particles size. It is worth noticing, that the introduction of non-magnetic Zn^{2+} ions into $NiFe_2O_4$ results in the migration of Fe^{3+} ions from A to B-sites, which causes the increase of the B-site magnetic moment and consequently an increase in the total magnetization (Bajorek et al., 2019). This could explain the higher saturation magnetization of the $Ni_{0.3}Zn_{0.7}Fe_2O_4$ ferrite when compared to that of $NiFe_2O_4$ ferrite in this study.

3.9. Scanning electron microscopy (SEM)

SEM images for the $NiFe_2O_4$ and $Ni_{0.3}Zn_{0.7}Fe_2O_4$ shown in Fig. 6 represents difference in the surface with particles agglomeration with diverse shapes and sizes. This difference in the SEM images signifies that the percentage of different ions Ni^{2+} and Zn^{2+} display an important role on the mesoporous structures of spinel ferrite synthesized.

3.10. Transmission electron microscopy (TEM)

TEM images for the $NiFe_2O_4$ and $Ni_{0.3}Zn_{0.7}Fe_2O_4$ shown in Fig. 7 represents difference of the agglomeration of weak interconnected particles with diverse shapes and sizes, where most of the particles appear spherical in shape however few elongated particles are also present in the images. This agglomeration state is probably related to the method of chemical synthesis adopted.

3.11. Acidity of the catalysts via –NH_3-TPD

The reactivity of the catalysts surface is a direct consequence of its intrinsic characteristics, as well as its synthesis method. However, the reactivity can be affected by conditions that are imposed on these materials to prepare them for a given application. Therefore, for a better accuracy of surface reactivity and to validate the claim that the materials are promising for catalysis, insight into the acidity and basicity of the catalyst

Table 7 Measurement of the magnetic parameters, obtained from the hysteresis curves of the $NiFe_2O_4$ and $Ni_{0.3}Zn_{0.7}Fe_2O_4$ ferrites.

Samples	Ms (emu/g)	Mr (emu/g)	Hc (G)	Mr/Ms
$NiFe_2O_4$	17.85	0.56	23.45	0.031
$Ni_{0.3}Zn_{0.7}Fe_2O_4$	31.50	1.78	48.83	0.056

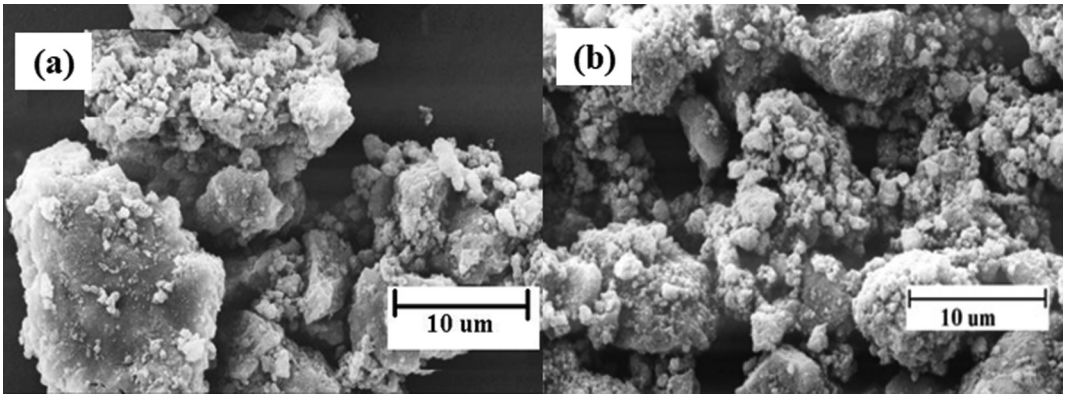

Fig. 6 SEM mesoporous structures of (a) $NiFe_2O_4$ and (b) $Ni_{0.3}Zn_{0.7}Fe_2O_4$ ferrites.

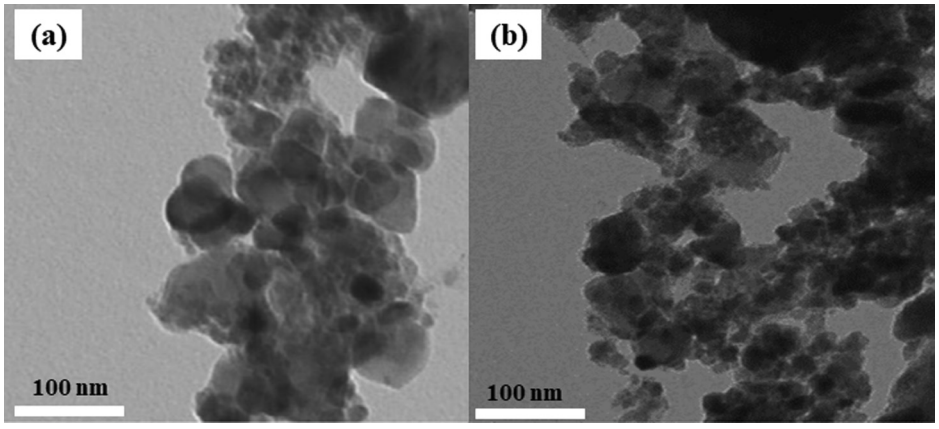

Fig. 7 Transmission electron microscopy (TEM) of (a) $NiFe_2O_4$ and (b) $Ni_{0.3}Zn_{0.7}Fe_2O_4$ ferrites.

is essential. The structural, morphological and surface reactivity characteristics exert a strong interaction with the nature, quantity and strength of the active sites (Dantas et al., 2017).

In catalysis, it is always necessary to determine the actually active surface, generally constituted by a set of atoms called sites, which have catalytic activity and because they are accessible to the reagents. Therefore, in the investigation of the acid sites, it was considered that the adsorption ammonia sites (NH_3) for the samples may be related to the interaction force with the acid sites, which are divided into weak, moderate and strong, according to the desorption event temperature NH_3. Adsorption sites of the weak type are those that occur in a temperature range of 10–200 °C, the moderate nature are those occurring from 100 to 350 °C and the strong nature those occurring from 350 to 500 °C (Dantas et al., 2017; Dantas et al., 2020).

Table 8 lists the results obtained from the TPD analysis. It should be noted that the final temperature results correspond to the average of three results obtained from $NiFe_2O_4$ and $Ni_{0.3}Zn_{0.7}Fe_2O_4$, as well as the volume of adsorbed NH_3 corresponds to the average of three results obtained from these samples after respective correction of the results, considering the deconvolution of the desorption peaks. Thus, the results show that the both samples are constituted of weak, moderate and strong acid sites. Almost 83% of the volumes of their sites of the $NiFe_2O_4$ ferrites are of a weak and moderate while for $Ni_{0.3}Zn_{0.7}Fe_2O_4$ ferrite, is about 57% of the volumes their sites are of a weak and moderate. Therefore, the results obtained from the TPD, where the desorption events of NH_3, considered as the acidic sites present in the samples, occurred at the final temperatures of 187, 309 and 478 °C with volumes of 2.12; 1.38 and 0.74 mL g^{-1} for $NiFe_2O_4$, and at 190, 305 and 445 °C with volumes of 1.42; 1.02 and 1.83 mL g^{-1} for $Ni_{0.3}Zn_{0.7}Fe_2O_4$, respectively.

Comparing the acid sites in the samples, we can say that the $Ni_{0.3}Zn_{0.7}Fe_2O_4$ had more acid sites of strong nature (43%) than $NiFe_2O_4$ with 17% of strong nature of the acid sites. This behavior is corroborated by the zeta potential and pH measurements results of the $NiFe_2O_4$ and $Ni_{0.3}Zn_{0.7}Fe_2O_4$ catalysts shown in Table 6.

3.12. Catalytic test during transesterification of soybean oil to biodiesel

Fig. 8 shows the obtained results of catalytic tests performed through the transesterification of soybean oil to biodiesel. Reported values are the results obtained from triplicate catalytic conversion experiments.

According to the conversions values shown in Fig. 8, it was observed that the reached result of 8.5% in the blank reagent, that is, the methyl transesterification reaction without the catalyst presence, shows the strong influence of the catalyst presence imposed on conversion of soybean oil to methyl esters, revealing the high performance of the samples studied as a catalyst for biodiesel production with yield values (effective conversion) of 49% for $NiFe_2O_4$ ferrite and in particular the sample $Ni_{0.3}Zn_{0.7}Fe_2O_4$, that is highlighted with an effective conversion of 94%. So probably the participation of these samples as a catalyst in methyl transesterification reactions of soybean oil was more effective and contribute to higher conversion values.

Table 8 Type of acidity present in $NiFe_2O_4$ and $Ni_{0.3}Zn_{0.7}Fe_2O_4$ ferrites.

Samples	Case	Final temperature (°C)	Volume (mL g^{-1})	Type of acidity
$NiFe_2O_4$	Case 1	187	2.12	Weak
	Case 2	309	1.38	Moderate
	Case 3	468	0.74	Strong
$Ni_{0.3}Zn_{0.7}Fe_2O_4$	Case 1	190	1.42	Weak
	Case 2	305	1.02	Moderate
	Case 3	445	1.83	Strong

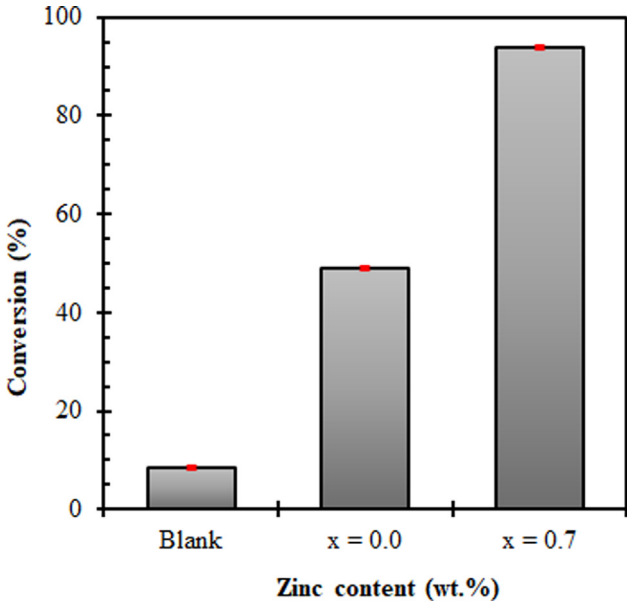

Fig. 8 Effect of the nanocatalysts $Ni_{1-x}Zn_xFe_2O_4$ (x = 0.0 and x = 0.7 mol of Zn^{2+} ions) on methyl ester conversion.

In addition, the results showed that the biodiesel conversion increased with an increase of Zn^{2+} ions from 49% for sample x = 0.0 to 94% for sample x = 0.7, showing that this catalyst was more active to biodiesel conversion. On the other hand, the presence of Zn^{2+} ions in $Ni_{1-x}Zn_xFe_2O_4$ system caused slightly a reduction in the surface area showing that this property was not responsible for the increase in catalytic activity. Also the Zn^{2+} ions caused an increase in the magnetic property, with a good saturation magnetization and strongly attracted by an external field (magnet) which favors and facilitates their recovery on the environment in which they are involved for later reuse. However, it was observed that the acidity and zeta potential, did affect the catalytic activity of the nanomagnetic catalysts for biodiesel production. Then, as reported in the TPD analysis, the sample x = 0.0 was the sample with the lowest active sites volume so that there was no satisfactory interaction between the involved reagents.

Other authors have reported the same behaviour. For example, Patil et al. (2014) concluded that the specific surface area is not the main factor that affects the catalytic activity, but probably other factors associated with the electron configuration, with the surface charges (zeta potential), with Lewis acid, as well as, with surface defects or atomic solid failures are decisive. In catalysis, the great advantage of magnetic nanoparticles is, among others, the high surface area of these materials; recovery; reusability via the use of the external magnetic field; and the presence of basic or acidic active sites that promote the catalytic processes (Dantas et al., 2017). Therefore, relating these magnetic properties, the increase of the zinc concentration was favorable for increasing the magnetization, zeta potential and acidity thus favoring the increase in catalytic activity.

Correlating the catalytic activity with zeta potential, it was observed that the more positive the value of the zeta potential implied higher catalytic performance. Hermes et al. (2014), have compared the photocatalytic oxidation of glycerol, using ZnO and TiO_2 and reported the same behavior.

The positive values of the zeta potential indicate the largest number of positive charges on the solid surface, which attract negative counter ions among them —OH group, which can thus capture the vacancy generating of catalysis, leading to the formation of *OH radicals responsible for indirect catalysis (Patil et al., 2014).

In this present study, the zeta potential indicated to be the most effective property that contributes to a catalytic performance of the sample $Ni_{0.3}Zn_{0.7}Fe_2O_4$ compared to $NiFe_2O_4$. Furthermore, the excellent catalytic activity was also directly related to the acidity characterized by TPD of NH_3 and pH values of the nanocatalysts $Ni_{0.3}Zn_{0.7}Fe_2O_4$, which became more acidic. This can be related to an increase in Lewis acidity due to presence of the zinc metal in composition. The catalytic activity was also related to the ease of polarizability of the Zn^{2+} ions compared to the Ni^{2+} ions ($Ni^{2+} < Zn^{2+}$). Therefore, the replacement of the nickel ion by zinc ion caused an increase of polarity due to the higher concentration of zinc ions. The same behavior was also observed by Sankaranarayanan et al. (2013) when investigated the catalytic properties of various types of AB_2O_4 ferrites synthesized by co-precipitation (A = Co, Ni, Cu and Zn and B = Fe) to the transesterification of vegetable oils with methanol to produce monoacid fatty esters (biodiesel).

Another possible explanation for the sample highlighted $Ni_{0.3}Zn_{0.7}Fe_2O_4$ to present a greater catalyst activity among the other tested samples can be the its morphology, consisting of agglomerates in the porous sponge form with high porosity in the agglomerates, may have contributed to a narrower interaction between the reaction agents, thus culminating in more satisfactory conversion result. The results of this study are corroborated by the authors Dantas et al. (2017) and Evangelista et al. (2016) where they reported that, although the research on the use of heterogeneous catalysts to obtain biodiesel is still in its early stages, it has obtained some interesting results, and the authors also added that in the context of the search for new heterogeneous catalysts, it is necessary development which is more efficient, cheaper, easier to prepare and are environmentally benign for large scale production.

It should also be point out that the biodiesel quality standard in Brazil is established by law; ANP Resolution 07/2008 and in the European Union; EN 14214. Both standards set minimum and maximum concentration values of different species present in produced biodiesel. The minimum ester content determined by Brazilian standard and the European standard is 96.5% of ester in biodiesel. Therefore, in this study, the maximum conversion of ester content obtained was 94% for $Ni_{0.3}Zn_{0.7}Fe_2O_4$ which is within the standards established by law. For sample $NiFe_2O_4$ ferrite, if the reactions conditions adopted are changed such as the molar ratio of alcohol: oil, amount of catalyst, time and temperature, those can be potential catalysts candidates to obtaining biodiesel with ester content within the standards established by law. Therefore, through this work it was possible to develop a final product with extensive application possibilities, thus fulfilling our objective of adding growth in the ceramic nanoscale a new material, with a relatively low cost, and mainly possibility of using a technological product directed to the society itself, regarding to the life and the environment preservation by contributing to the biodiesel production, in order to fulfil the true science role, which is to promote the common good of society in general.

4. Conclusions

$NiFe_2O_4$ and $Ni_{0.3}Zn_{0.7}Fe_2O_4$ magnetic nanoparticles were synthesized via combustion reaction method. The XRD results confirmed the crystalline nature and presence of single-phase spinel structure. The presence of Zn^{2+} ions affected mainly in the reduction of the surface area and this increased in the magnetic property, acidity and zeta potential. Catalytically, the magnetic nanoferrites displayed a maximum conversion of 94% during the transesterification of soybean oil to biodiesel. Consequently, results documented in this study have strengthened the catalytic potential of $NiFe_2O_4$ and $Ni_{0.3}Zn_{0.7}Fe_2O_4$ magnetic nanoparticles in the production of biodiesel. In addition, this use of these catalyst could be instrumental to reducing the recovery cost associated with the production of biodiesel via homogeneous catalysis and thus promote the development environmentally benign largescale biodiesel.

Declaration of Competing Interest

The authors declare no conflicts of interest.

Acknowledgements

The authors thank PNPD/CAPES, process number [23038.007104/2011-84], AUX PE – PNPD – 2490/2011 and CNPq process number [404395/2013-9] and process number [402029/2013-5], MCTM/CNPq process number [190822/2013-9] for financial support.

References

Abbas, M.K., Khan, M.A., Mushtaq, F., Warsi, M.F., Sher, M., Shakir, I., AlyAboud, M.F., 2017. Impact of Dy on structural, dielectric and magnetic properties of Li-Tb-nanoferrites synthesized by micro-emulsion method. Ceram. Int. 43, 5524–5533.

Abu-Reziq, R., Alper, H., Wang, D.S., Post, M.L., 2006. Metal supported on dendronized magnetic nanoparticles: high selective hydroformulation catalysts. J. Am. Chem. Soc. 128, 5279–5282.

Ajmal, M., Maqsood, A., 2007. Influence of zinc substitution on structural and electrical properties of $Ni_{1-x}Zn_xFe_2O_4$ ferrites. Mater. Sci. Eng. 139, 164–170.

Amiri, G.R., Yousefi, M.H., Abolhassani, M.R., Manouchehri, S., Keshavarz, M.H., Fatahian, S., 2011. Magnetic properties and microwave absorption in Ni–Zn and Mn– Zn ferrite nanoparticles synthesized by low-temperature solid-state reaction. J. Magn. Magn. Mater. 323, 730–734.

Andjelković, L., Šuljagić, M., Lakić, M., Jeremić, D., Vulić, P., Nikolić, A.S., 2018. A study of the structural and morphological properties of Ni–ferrite, Zn–ferrite and Ni–Zn–ferrites functionalized with starch. Ceram. Int. 44, 14163–14168.

Andrade, H.M.C., Costa, A.C.F.M., Lula, R.P.T., Kiminami, R.H.G.A., Vieira, L.G.F., Jesus, A.A., 2005. Preparation of ferrite nickel catalysts by combustion reaction. J. Mater. Sci. 2, 25.

Azadmanjiri, J., 2008. Structural and electromagnetic properties of Ni–Zn ferrites prepared by sol–gel combustion method. Mater. Chem. Phys. 109, 109–112.

Bajorek, A., Berger, C., Dulski, M., Łopadczak, P., Zubko, M., Prusik, K., Wojtyniak, M., Chrobak, A., Grasset, F., Randrianantoandro, N., 2019. Microstructural and magnetic characterization of $Ni_{0.5}Zn_{0.5}Fe_2O_4$ ferrite nanoparticles. J. Phys. Chem. Solids 129, 1–21.

Barakos, N., Pasias, S., Papayannakos, N., 2008. Transesterification of triglycerides in high and low quality oil feeds over an HT2 hydrotalcite catalyst. Bioresour. Technol. 99, 5037–5042.

Bercoff, P.G., Bertorello, H.R., 2000. Localized canting effect in Zn-substituted Ni ferrites. J. Magn. Magn. Mater. 213, 56–62.

Buschow, K.H.J., De Boer, F.R., 2003. Physics of Magnetism and Magnetic Materials. Kluwer Academic, New York.

Cai, W., Fu, C., Hu, W., Chen, G., Deng, X., 2013. Effects of microwave sintering power on microstructure, dielectric, ferroelectric and magnetic properties of bismuth ferrite ceramics. J. Alloy. Compd. 554, 64–71.

Chatterjee, A., Das, D., Pradhan, S.K., Chakravorty, D., 1993. Synthesis of Nanocrystalline nickel–zinc ferrite by the sol–gel method. J. Magn. Magn. Mater. 127, 214–218.

Chen, D.H., He, X.R., 2001. Synthesis of nickel ferrite nanoparticles by sol–gel method. Mater. Res. Bull. 36, 1369–1377.

Chen, C., Zuo, W.Q., Yang, J.C.E., Cui, H.J., Fu, M.L., 2016. Yolk–shell structured $CoFe_2O_4$ microspheres as novel catalysts for peroxymonosulfate activation for efficient degradation of butyl paraben. : RSC Adv. 6, 10136.

Costa, A.C.F.M., Kiminami, R.H.G.A., 2012. Dispositivo para produção de nanomateriais cerâmicos em larga escala por reação de combustão e processo contínuo de produção dos nanomateriais. Depósito de patente. Revista de Propriedade Industrial – RPI, patente n° BR 10 2012 002181-3.

Costa, A.C.F.M., Morelli, M.R., Kiminami, R.H.G.A., 2002a. Combustion synthesis: effect of urea on the reaction and characteristics of Ni-Zn ferrite powders. J. Mater. Synth. Process. 9, 347–352.

Costa, A.C.F.M., Tortela, E., Morelli, M.R., Kiminami, R.H.G.A., Kaufman, M.R., 2002b. Effect of heating conditions during combustion synthesis on the characteristics of $Ni_{0.5}Zn_{0.5}Fe_2O_4$ nanopowders. J. Mater. Sci. 37, 3569–3572.

Costa, A.C.F.M., Tortela, E., Morelli, M.R., Kiminami, R.H.G.A., 2003. Ni-Zn ferrite nanoparticles prepared by combustion reaction. Mater. Sci. Forum 416–18, 699–704.

Costa, A.C.F.M., Kiminami, R.H.G.A., Morelli, M.R., 2009. Combustion synthesis processing of nanoceramics. In: Handbook of Nanoceramics and Their Based Nanodevices (Synthesis and Processing), vol. 1. American Scientific Publishers, pp. 375–392.

Dantas, J., Silva, A.S., Santos, P.T.A., Santos, J.R.D., Barbosa, D.C., Meneghetti, S.M.P., 2012. Evaluation of catalyst $Ni_{0.4}Cu_{0.1}Zn_{0.5}$-Fe_2O_4 on methyl esterification of free fatty acid present in cottonseed oil. Mater. Sci. Forum. 727–728, 1302–1307.

Dantas, J., Santos, J.R.D., Cunha, R.B.L., Kiminami, R.H.G.A., Costa, A.C.F.M., 2013. Use of Ni-Zn ferrites doped with Cu as catalyst in the transesterification of soybean oil to methyl esters. Mater Res. 16, 625–627.

Dantas, J., Leal, E., Mapossa, A.B., Cornejo, D.R., Costa, A.C.F.M., 2017. Magnetic nanocatalysts of $Ni_{0.5}Zn_{0.5}Fe_2O_4$ doped with Cu and performance evaluation in transesterification reaction for biodiesel production. Fuel 191, 463–471.

Dantas, J., Leal, E., Cornejo, D.R., Kiminami, R.H.G.A., Costa, A.C.F.M., 2020. Biodiesel production evaluating the use and reuse of magnetic nanocatalysts $Ni_{0.5}Zn_{0.5}Fe_2O_4$ synthesized in pilot-scale. Arab. J. Chem. 13, 3026–3042. https://doi.org/10.1016/j.arabjc.2018.08.012.

Das, P.S., Singh, G.P., 2016. Structural, magnetic and dielectric study of Cu substituted NiZn ferrite nanorod. J. Magn. Magn. Mater. 401, 918–924.

David, J., 1998. Introduction to Magnetism and Magnetic Materials. Chapman & Hall, London [xxvii, p. 536].

De Medeiros, I.A.F., Lopes-Moriyama, A.L., de Souza, C.P., 2017. Effect of synthesis parameters on the size of cobalt ferrite crystallite. Ceram. Int. 43, 3962–3969.

Deepty, M., Srinivasa, C., Kumar, R.E., Mohan, K.N., Prajapat, C.L., Rao, C.T.V., Meena, S.S., Verma, A.K., Sastry, D.L., 2019. XRD, EDX, FTIR and ESR spectroscopic studies of co-precipitated Mn–substituted Zn–ferrite nanoparticles. Ceram. Int. 45, 8037–8044.

Degirmenbasi, N., Coskun, S., Boz, N., Kalyon, D.M., 2015. Biodiesel synthesis from canola oil via heterogeneous catalysis using functionalized CaO nanoparticles. Fuel 153, 620–627.
Derek, C., 1998. Magnetism: Principles and Applications. Wiley, New York [p. 459, ISBN 047195417-9].
Diniz, A.P.A., Gama, L., Morelli, M.R., Kiminami, R.H.G.A., Costa, A.C.F.M., 2004. Comparation of Ni-Zn ferrite powder preparation by combustion reaction using different synthetization routes. J. Metastable Nanocryst. Mater. 20–21, 582–587.
Dzunuzovic, A.S., Ilic, N.I., Petrovic, M.M.V., Bobic, J.D., Stojadinovic, B., Mitrovic, Z.D., Stojanovic, B.D., 2015. Structure and properties of Ni–Zn ferrite obtained by auto-combustion method. J. Magn. Magn. Mater. 374, 245–251.
EL-Sayed, A.M., 2002. Influence of zinc content on some properties of Ni-Zn ferrites. Ceramics Int. 28, 363–367.
Evangelista, J.P.C., Gondim, A.D., Souza, L.D., Araújo, A.S., 2016. Alumina-supported potassium compounds as heterogeneous catalysts for biodiesel production: a review. Renew. Sustain. Energy Rev. 59, 887–894.
Feitoza, N.C., Gonçalves, T.D., Mesquita, J.J., Menegucci, J.S., Santos, M.K.M.S., Chaker, J.A., Cunha, R.B., Medeiros, A.M.M., Rubim, J.C., Sousa, M.H., 2014. Fabrication of glycine-functionalized maghemite nanoparticles for magnetic removal of copper from wastewater. J. Hazard. Mater. 264, 53–160.
Gabal, M.A., Kosa, S., ElMuttairi, T.S., 2014. Magnetic dilution Effect of nano-crystalline $NiFe_2O_4$ synthesized via sucrose-assisted combustion route. Ceram. Int. 40, 675–681.
Gao, P., Hua, X., Degirmenci, V., Rooney, D., Khraisheh, M., Pollard, R., Bowman, R.M., Rebrov, E.V., 2013. Structural and magnetic properties of $Ni_{1-x}Zn_xFe_2O_4$ (x = 0.0; 0.5 e 1.0) nanopowders prepared by sol–gel method. J. Magn. Magn. Mater. 348, 44–50.
Goldman, A., 1993. Modern Ferrite Technology. Marcel Dekker, New York.
Gorter, E.W., 1954. Saturation magnetization and crystal chemistry of ferromagnetic oxides. Philips Res. Rep. 9, 295–320.
Gul, I.H., Ahmed, W., Maqsood, A., 2008. Electrical and magnetic characterization of nanocrystalline Ni-Zn ferrite synthesis by co-precipitation route. J. Magn. Magn. Mater. 320, 270–275.
Guo, L., Shen, X., Meng, X., Feng, Y., 2010. Effect of Sm^{3+} ions doping on structure and magnetic properties of nanocrystalline $NiFe_2O_4$ fibers. J. Alloy. Compd. 490 (1–2), 301–306.
Gupta, N., Verma, A., Kashyap, S.C., 2007. Micro structural, dielectric and magnetic behavior of spin deposited nanocrystalline nickel-zinc ferrite thin films for microwave applications. J. Magn. Magn. Mater. 308, 137–142.
Gurunathan, B., Ravi, A., 2015. Process optimization and kinetics of biodiesel production from neem oil using copper doped zinc oxide heterogeneous nanocatalyst. Bioresour. Technol. 190, 424–428.
Hajalilou, A., Mazlan, S.A., 2016. A review on preparation techniques for synthesis of nanocrystalline soft magnetic ferrites and investigation on the effects of microstructure features on magnetic properties. Appl. Phys. A Mater. Sci. Process. 122, 1–15.
Hazra, S., Ghosh, N.N., 2014. Preparation of nanoferrites and their applications. J. Nanosci. Nanotechnol. 14, 1983–2000.
Hermes, N.A., Corsetti, A., Lansarin, M.A., 2014. Comparative study on the photocatalytic oxidation of glycerol using ZnO and TiO_2. Chem. Latt.. 43, 143–145.
Hwang, C.C., Tsai, J.S., Huang, T.H., Peng, C.H., Chen, S.Y., 2005. Combustion synthesis of Ni-Zn ferrite powder – influence of oxygen balance value. J. Solid- State Chem. 178, 382–389.
Klung, H., Alexander, L., 1962. X-Ray Diffraction Procedures. Wiley, New York, EUA, p. 491.
Koekkoek, A.J.J., Veen, J.A.B.V., Gerrtisen, P.B., Giltay, P., Magusin, P.C.M.M., Hensen, E.J.M., 2012. Brønsted acity of AI/SBA-15. Microporus Mesoporus Mater. 151, 34–43.
Korichi, S., Elias, A., Mefti, A., Bensmaili, A., 2012. The effect of microwave irradiation and conventional acid activation on the textural properties of smectite: Comparative study. Appl. Clay Sci. 59–60, 76–83.
Liu, Y., Li, J., Min, F., Zhu, J., Zhang, M., 2014. Microwave-assisted synthesis and magnetic properties of $Ni_{1-x}Zn_xFe_2O_4$ ferrite powder. J. Magn. Magn. Mater. 354, 295–298.
Liu, Y., Zhang, P., Fan, M., Jiang, P., 2016. Biodiesel production from soybean oil catalyzed by magnetic nanoparticle $MgFe_2O_4$@CaO. Fuel 164, 314–321.
Lopez, D.E., Goodwin Jr, J.G., Bruce, D.A., Lotero, E., 2005. Transesterification of triacetin with methanol on solid acid and base catalysts. Appl. Catal. A – General. 295, 97–105.
Masrour, R., El Moussaoui, H., Salmani, E., Mounkachi, O., Ez-Zahraouy, H., Hamedoun, M., Hlil, E.K., Benyoussef, A., 2014. Synthesis and magnetic properties of bulk ferrites spinels $Ni_{0.5}Zn_{n0.5}F_e2_O4$: Experimental an Ab-Initio study. J. Supercond. Novel Magn. 27 (1), 177–181.
Morrish, A.H., 1995. The Physical Principles of Magnetism. John Wiley and Sons, New York.
Murugesan, C., Perumal, M., Chandrasekaran, G., 2014. Structural, dielectric and magnetic properties of cobalt ferrite prepared using auto-combustion and ceramic route. Phys. B 448, 53–56.
Nyutu, E.K., Conner, W.C., Auerbach, S.M., Chen, C.H., Suib, S.L., 2008. Ultrasonic nozzle spray in situ mixing and microwave-assisted preparation of nanocrystalline spinel metal oxides: nickel ferrite and zinc aluminate. J. Phys. Chem. C 112 (5), 1407–1414.
O'handley, R.C., 2000. Modern Magnetic Materials: Principles and Applications. Wiley, New York [p. 740, Includes bibliographical references and index, ISBN 978047115669].
Patil, R.S., Kokate, M.R., Shinde, D.V., Kolekar, S.S., Han, S.H., 2014. Synthesis and enhancement of photocatalytic activities of ZnO by silver nanoparticles. Spectrochimica Acta Part A: Mol. Biomol. Spectrosc. 122, 113–117.
Ping, R., Junxi, Z., Huiyong, D., 2009. Preparation and microstructure of spinel zinc ferrite $ZnFe_2O_4$ by co-precipitation method. J. Mater. Sci. 24, 927–930.
Prasad, S., Gajbhiye, N.S., 1998. Magnetic studies of nanosized nickel ferrite particles synthesized by citrate precursor technique. J. Alloy. Compd. 265, 87–92.
Reed, J.S., 1995. Principles of Ceramics Processing. John Wiley & Sons Inc, New York, NY.
Rezlescu, N., Rezlescu, E., Popa, P.D., Doroftei, C., Ignat, M., 2013. Preparation and characterization of spinel-type $MeFe_2O_4$ (Me = Cu, Cd, Ni and Zn) for catalyst applications. Mater. Chem. Phys. 137, 922–927.
Rouquerol, F., Rouquerol, J., Sing, K., 1999. Adsorption by Powders & Porous Solids. Principles, Methodology and Applications. New York.
Sankaranarayanan, T.M., Shanthi, R.V., Thirunavukkarasu, K., Pandurangan, A., Sivasanker, S., 2013. Catalytic properties of spinel-type mixed oxides in transesterification of vegetable oils. J. Mol. Catal. A: Chem. 379, 234–242.
Santos, P.T.A., Costa, A.C.F.M., Andrade, H.M.C., 2012. Preparation of $NiFe_2O_4$ and $ZnFe_2O_4$ samples by combustion reaction and evaluation of performance in reaction water gas shift reaction – WGSR. Mater. Sci. Fórum. 727–728, 1290–1295.
Satheeshkumar, M.K., Ranjith Kumar, E., Srinivas, Ch., Prasad, G., Meena, S.M., Pradeep, I., Suriyanarayanan, N., Sastry, D.L., 2019. Structural and magnetic properties of $CuFe_2O_4$ ferrite nanoparticles synthesized by cow urine assisted combustion method. J. Magn. Magn. Mater. 484, 120–125.
Segadães, A.M., Morelli, M.R., Kiminami, R.H.G.A., 1998. Combustion synthesis of aluminium titanate. J. Eur. Ceram. Soc. 8, 771–781.
Seo, J.Y., Lee, K., Lee, S.Y., Jeon, S.G., Na, J.-G., Oh, Y.-K., 2014. Effect of barium ferrite particle size on detachment efficiency in magnetophoretic harvesting of oleaginous Chlorella sp. Bioresour. Technol. 152, 562–566.
Shafi, K., Koltypin, Y., Gedanken, A., Prozorov, R., Balogh, J., Lendvai, J., Felner, I., 1997. Sonochemical preparation of nano-

sized amorphous $NiFe_2O_4$ particles. J. Mater. Chem. Phys. 101, 6409–6414.
Shahane, G.S., Kumar, A., Arora, M., Pant, R.P., Lal, K., 2010. Synthesis and characterization of Ni-Zn ferrite nanoparticles. J. Magn. Magn. Mater. 322, 1015–1019.
Shanmugavel, T., Gokul, R.S., Rajarajan, G., Kumar, G.R., 2014. Tailoring the structural and magnetic properties and of nickel ferrite by auto combustion method. Procedia Mater. Sci. 6, 1725–1730.
Shi, Y., Ding, J., Liu, X., Wang, J., 1999. $NiFe_2O_4$ ultrafine particles prepared by co-precipitation/mechanical alloying. J. Magn. Magn. Mater. 205, 249–254.
Shylesh, S., Schweizer, J., Demeshko, S., Schunemann, V., Ernest, S., Thiel, W.R., 2009. Nanoparticles supported, magnetically recoverable oxodipero molybdenum complexes: efficient catalysts for selective epoxidation reactions. Adv. Synth. Catal. 351, 1789–1795.
Sing, K.S.W., Everett, D.H., Haul, R.A.W., Moscou, L., Pierotti, R. A., Rouquerol, J., Siemieniewska, T., 1985. Reporting physisorption data for gas/solid systems with special reference to the determination of surface area and porosity. Pure Appl. Chem. 57, 603–619.
Sivakumar, P., Ramesh, R., Ramanand, A., Ponnusamy, S., Muthamizhchelvan, C., 2011. Preparation and properties of nickel ferrite ($NiFe_2O_4$) nanoparticles via sol–gel auto-combustion method. Mater. Res. Bull. 46, 2204–2207.
Sundararajan, R., Srinivasan, V., 1991. Catalytic decomposition of nitrous oxide on $Cu_xCo_{3-x}O_4$ spinels. Appl. Catal. 73, 165–171.
Sutka, A., Strikis, G., Mezinskis, G., Lusis, A., Zavickis, J., Kleperis, J., Jakovlevs, D., 2012. Properties of Ni–Zn ferrite thin films deposited using spray pyrolysis. Thin Solid Films 526, 65–69.
Syue, M.R., Wei, F.J., Chou, C.S., Fu, C.M., 2011. Magnetic, dielectric, and complex impedance properties of nanocrystalline Mn–Zn ferrites prepared by novel combustion method. Thin Solid Films 519, 8303–8306.
Tholkappiyan, R., Vishista, K., 2014. Synthesis and characterization of barium zinc ferrite nanoparticles: working electrode for dye sensitized solar cell applications. Sol. Energy 106, 118–128.
Vieira, D.A., Diniz, V.C.S., Cornejo, D.R., Costa, A.C.F.M., Kiminami, R.H.G.A., 2014. Study of the reproducibility of Ni-Zn nanoferrite obtained by combustion reaction. Mater. Sci. Forum 775–776, 415–420.
Waldron, R.D., 1955. Infrared spectra of ferrites. Phys. Rev. 99, 1727–1735.
Xie, L., Ren, X., Liu, Q., Cui, G., Ge, R., Asiri, A.M., Sun, X., Zhang, Q., Chen, L., 2018. A Ni $(OH)_2$–PtO_2 hybrid nanosheet array with ultralow Pt loading toward efficient and durable alkaline hydrogen evolution. J. Mater. Chem. A 6, 1967–1970.
Yang, J.M., Tsuo, W.J., Yen, F.S., 1999. Preparation of ultrafine nickel ferrite powders using mixed Ni and Fe tartrates. J. Solid State Chem. 145, 50–57.
Yang, L., Wu, T., Zhang, R., Zhou, H., Xia, L., Shi, X., Zheng, H., Zhang, Y., Sun, X., 2019. Insights into defective TiO_2 in electrocatalytic $_N2$ reduction: combining theoretical and experimental studies. Nanoscale 11, 1555–1562.
Zhang, P., Han, Q., Fan, M., Jiang, P., 2014. Magnetic solid base catalyst $CaO/CoFe_2O_4$ for biodiesel production: influence of basicity and wettability of the catalyst in catalytic performance. Appl. Surf. Sci. 317, 1125–1130.
Zhang, C.Y., Shen, X.Q., Zhou, J.X., Jing, M.X., Cao, K., 2007. Preparation of spinel ferrite $NiFe_2O_4$ fibres by organic gel-thermal decomposition process. J. Sol-Gel Sci. Technol. 42 (1), 95–100.
Zhang, P., Shi, M., Liu, Y., Fan, M., Jiang, P., Dong, Y., 2016. Sr doping magnetic CaO parcel ferrite improving catalytic activity on the synthesis of biodiesel by transesterification. Fuel 186, 787–791.
Zhang, Y., Stangle, Y.G.C., 1994. Preparation of fine multicomponent oxide ceramic powder by a combustion synthesis process. J. Mater. 9, 1997–2004.
Zhang, L., Xie, X.Y., Wang, H., Ji, L., Zhang, Y., Chen, H., Li, T., Luo, Y., Cui, G., Sun, X., 2019. Boosting electrocatalytic $_N2$ reduction by Mn_O2 with oxygen vacancies. Chem. Commun. 55, 4627–4630.
Zhao, J., Li, X., Cui, G., Sun, X., 2018. Highly-active oxygen evolution electrocatalyzed by an Fe-doped $NiCr_2O_4$ nanoparticle film. Chem. Commun. 54, 5462–5465.
Zhong, Y., Zhongwen, L.A.N., Shengming, C., 2006. Microstructure and magnetic properties of Ni substituted high-density Mn-Zn ferrites. Rare Metals 25, 584–587.